

LAMPSS: Discovery of Metal-Poor Stars in the Galactic Halo with the CaHK filter on CFHT MegaCam ^{*}

Eleanor Worrell¹, Niam Patel¹, Karolina Wresilo¹, Sam Dicker¹, Olivia Bray¹
 Jack Bagness¹ & David Sobral¹†

¹ Department of Physics, Lancaster University, Lancaster, LA1 4YB, UK

Accepted 31 May 2019. Received 31 May 2019; in original form 25 March 2019

ABSTRACT

We present the Lancaster Astrophysics Metal Poor Star Search (*LAMPSS*) in the Milky Way halo, conducted using the metallicity-sensitive Ca H & K lines. We use the CaHK filter of the MegaPrime/MegaCam on the Canada-France-Hawaii Telescope (CFHT) to survey an area of 1.010deg² over the COSMOS field. We combine our new CaHK data with broadband optical and near-infrared photometry of COSMOS to recover stars down to $m_{\text{HK}} \sim 26$. After removing galaxies, we find 70% completion and 30% contamination for our remaining 1772 stars. By exploring a range of spectral types and metallicities, we derive metallicity-sensitive colour-colour diagrams which we use to isolate different spectral types and metallicities ($-5 \leq [\text{Fe}/\text{H}] \leq 0$). From these, we identify 16 potentially extremely metal-poor stars. One of which, LAMPS_1229, we predict to have $[\text{Fe}/\text{H}] \sim -5.0$ at a distance of (78.21 ± 9.37) kpc. We construct a Metallicity Distribution Function for our sample of metal-poor stars, finding an expected sharp decrease in count as $[\text{Fe}/\text{H}]$ decreases.

Key words: Galaxy: Halo - Stars: Population III - stars: abundances - Galaxy: evolution - Galaxy: Archaeology

1 INTRODUCTION

The Λ CDM model suggests the Universe can be traced back to a singularity 13.8 Gyrs ago (Lemaître 1927; Macaulay et al. 2018). Several hundred million years after, the first stars formed. These Population III stars would have been composed entirely of primordial gas (hydrogen, helium and trace amounts of beryllium and lithium). The existence of Population III stars is expected, as heavy elements present in the Universe can only be synthesised in the interior of stars. It has long been thought that these first generation stellar Populations would be exclusively high mass stars ($\sim 100M_{\odot}$) (e.g. Bromm et al. 1999; Schaerer 2002). However, more recently it has been simulated that the metal-free clouds of the early Universe would allow protostars of $0.1M_{\odot}$ (e.g. Becerra et al. 2015; Stacy et al. 2016) and that the primordial IMF may extend below $0.8M_{\odot}$ (e.g. Hartwig et al. 2015). At those masses, stellar lifetimes are greater than cosmic time so Population III stars could still be observable on the

main sequence today. The *Caterpillar* simulation suite predicts that a Milky Way-like host galaxy would have many Population III formation sites at $z \sim 25$ (e.g. Griffen et al. 2018), meaning there is the exciting possibility that Population III stars may have formed in, and still be present in, our galactic halo. Direct observation of a Population III star would be of great significance for various areas of astrophysics and cosmology. Firstly, it allows unparalleled access to nucleosynthesis within the very first generation of stars which can help validate current knowledge of stellar nucleosynthesis. It has been predicted, via simulations, that a significant portion of galaxies are “Population III - bright” immediately prior to the epoch of reionisation (Sarmiento et al. 2018). Therefore, understanding Population III stars is a crucial step in fully understanding the epoch of reionisation in the Universe (Koh & Wise 2018). Furthermore, observing a Population III star would constrain the IMF of Population III stars which is currently uncertain. It would also provide insight into the formation of the proto-Milky Way as well as any accretion events in our galaxy’s history (e.g. Sestito et al. 2019).

* Based on Cosmic Evolution Survey (COSMOS) data, CaHK CFHT data (programs 15BC10, 16A038 & 17BO54 PI: Sobral), theoretical spectral models provided by POLLUX, and images from the *HST*.

† PHYS369 supervisor.

Metallicity is defined as the mass fraction, Z , of elements heavier than helium in the star. Therefore, Population III stars should theoretically have zero metallicity. Further-

more, massive Population III stars can go supernovae within just a few million years, releasing metals into the Universe for the first time. These metals are then available to go on to form early Population II stars which should also be very low in metals. Metallicity is commonly quantified by the ratio of iron to hydrogen within a star, $[\text{Fe}/\text{H}]$. $[\text{Fe}/\text{H}]$ represents a logarithmic comparison of this ratio with respect to the solar ratio. Metal-poor stars are classified as follows; extremely, ultra, and hyper metal-poor (EMP, UMP and HMP hereafter) stars with $[\text{Fe}/\text{H}] < -3.0$, $[\text{Fe}/\text{H}] < -4.0$, and $[\text{Fe}/\text{H}] < -5.0$, respectively (Beers & Christlieb 2005).

Several metal-poor star studies have been conducted. One of the most recent is the *Pristine* survey (Starkenburg et al. 2017), a narrow-band survey which used the metallicity-sensitive Ca H & K lines (CaHK hereafter), which lie at 3968.47Å and 3933.66Å respectively. The success and potential of the survey at identifying EMPs is unprecedented, with the survey having already confirmed one of the most metal-poor stars found, *Pristine* 221.8781+9.7844 with $[\text{Fe}/\text{H}] = -4.66 \pm 0.13$ (Starkenburg et al. 2018). Broad-band photometric surveys can also identify metal-poor stars, such as SDSS J102915+172927, the Caffau dwarf star, with $[\text{Fe}/\text{H}] = -4.5$ (Caffau et al. 2011). The most iron deficient star is the *Skymapper* Southern Sky Survey star SMSS J031300.36 - 670839.3 which has $[\text{Fe}/\text{H}] < -6.53$ (Keller et al. 2014; Nordlander et al. 2017). Recently, restrictions in metal-poor star studies due to small sample size have been lifted as many more metal-poor stars are found, for example, the hundreds of new metal-poor stars identified by the R-process Alliance from *RAVE* data (Sakari et al. 2018; Hansen et al. 2018). Furthermore, future Population III searches have been proposed, where pair-instability supernovae could be used as a high redshift probe (e.g. Hartwig et al. 2018).

Another major problem in the search for primordial stars thus far, is that the majority of metal-poor stars are carbon enhanced (CEMP), such as the stars G64-12 and G64-37 (Placco et al. 2016a). However, UMP stars without enhanced carbon abundance have been found, such as *Pristine* 221.8781+9.7844 and the Caffau star. Additionally, it has been found that in the Sagittarius dwarf galaxy there exists a very metal-poor stellar population and that out of four newly identified stars, none are CEMP stars (Chiti & Frebel 2019). Further work has suggested that multiple stellar progenitors are required at $[\text{Fe}/\text{H}] -4.0$ (e.g. Placco et al. 2016b), meaning multiple formation routes for UMP stars.

Numerical simulations suggest that the halo is the most likely place to find Population III survivors (e.g. Ishiyama et al. 2016; Magg et al. 2018). It follows that the Population III stars most likely to have escaped enrichment from supernovae winds will be towards the outskirts of the halo. In this report we present one of the first attempts to probe the extra-galactic field for metal-poor stars, using the narrow-band CaHK filter of the MegaPrime/MegaCam on the Canada-France-Hawaii Telescope (CFHT) in combination with the broad-band optical and near-infrared photometry available in the COSMOS field. We survey 1.010 deg² of sky in the northern hemisphere to ~ 26 mag, 5 magnitudes deeper than the aforementioned *Pristine* survey.

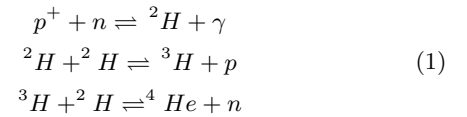
This report is organised as follows. §2 gives background on Population III stars. In §3 we present the sample, drawn from the COSMOS catalogue with CaHK data from CFHT.

The methods used to reduce the initial *LAMPSS* catalogue, as well as the construction of metallicity-sensitive colour-colour diagrams, are both presented in §4. In §5 we present the 16 EMP candidates identified and give stellar number densities per spectral type per metallicity for the region surveyed. Throughout this paper we use AB magnitudes (Oke & Gunn 1983).

2 THEORETICAL BACKGROUND

2.1 Composition of Population III Stars

Once the temperature of the Universe dropped to 10⁹ K, fusion of hydrogen, deuterium, tritium and helium could occur via the processes shown in Equation 1¹. Heavier elemental isotopes were unable to form in the recombination epoch². Helium has too great a Coulomb barrier compared to the kinetic energy available (which drops with temperature as the Universe expands), for helium fusion to occur.



Another factor that inhibits production of elements heavier than helium before first generation stars, is the suppression of neutron capture due to neutron decay and the expansion of the Universe. Neutron capture, which is the first process shown in Equation 1, is a necessary step in the fusion of helium-4, as shown above in Equation 1. The half-life of a free neutron is approximately 10 minutes, therefore any free neutron would quickly decay into a proton and electron, making the chance of a stable helium nuclei significantly less likely³. After inflation, the rate of the expansion of the Universe has been accelerating (e.g. Scharping 2017), decreasing the density of matter with time from the recombination epoch. This meant neutron capture, and thereby production of heavier elements, would get exponentially less likely as time advances until other methods of nucleosynthesis are viable.

Elements heavier than helium can only be generated through stellar nucleosynthesis and supernovae (Ryan & Norton 2010), where the temperature is such that particles have sufficient energy to overcome the Coulomb barrier of the helium nuclei. As a result, the primordial Population III stars are composed of only hydrogen and helium with trace amounts of lithium.

2.2 Why are Population III stars elusive?

There are several complications when searching for Population III stars. The age of any surviving Population III stars is of the order of cosmic time, so by looking at Table 1, it is almost certain that the majority of Population III stars will have long since left the main sequence and completed their

¹ <http://burro.case.edu/Academics/Astr222/Cosmo/Early/bbn.html>

² <http://abyss.uoregon.edu/~js/ast123/lectures/lec21.html>

³ https://wmap.gsfc.nasa.gov/Universe/bb_tests_ele.html

Spectral Type	Colour	Temperature (K)	Main Sequence Lifetime
O	Blue	>30,000	<5 Myrs
B	Blue	11,000 - 30,000	5 - 800 Myrs
A	Light Blue	7,500 - 11,000	800 Myrs - 3 Gyrs
F	White	6,000 - 7,500	3 - 8 Gyrs
G	Yellow	5,000 - 6,000	8 - 18 Gyrs
K	Orange	3,500 - 5,000	18 - 50 Gyrs
M	Red	<3,500	>50 Gyrs

Table 1. Main sequence lifetimes of spectral types, calculated in Appendix ??.

evolution. Especially since it is predicted that the majority of Population III stars were much larger than later stellar generations ($M \gtrsim 100 M_{\odot}$) (Stacy et al. 2016), which have lifetimes of ~ 10 Myrs (e.g. Weidner & Vink 2010). Hence, they now would be observed as remnants such as neutron stars or black holes. The original composition of these remnants is increasingly difficult to determine due to the loss or consumption of internal elements during the process of stellar evolution (e.g. Laughlin et al. 1997).

There is also the potential that low mass Population III stars have become contaminated with heavier elements when moving through the ISM, altering the composition of the outer layers. Population III stars may undergo a process known as self-contamination through the dredge up of products of stellar nucleosynthesis in the core, causing the appearance of a higher metallicity, typically associated with Population II stars⁴.

2.3 Metallicity Determination and Fraunhofer Lines

If metals are present in the stellar atmosphere, it is possible to determine the stars' metallicity through analysis of their spectra. Elements display their own characteristic absorption lines and hence they can be easily identified. As photons travel through the stellar envelope they can be captured by atoms if the photon has energy equal to the difference in energy between 2 energy states of that atom. When this light is re-emitted in all directions, the overall light intensity at that particular wavelength decreases causing a distinctive absorption lines. Stellar metallicity is typically defined by $[\text{Fe}/\text{H}]$; a logarithmic ratio of the abundance of iron relative to hydrogen.

$$[\text{Fe}/\text{H}] = \log_{10} \left(\frac{N_{\text{Fe}}}{N_{\text{H}}} \right)_{*} - \log_{10} \left(\frac{N_{\text{Fe}}}{N_{\text{H}}} \right)_{\odot} \quad (2)$$

Here, N_{Fe} and N_{H} represent the number densities of iron and hydrogen atoms, respectively. The logarithmic metallicity of a star is compared to that of the Sun, such that the more negative the ratio $[\text{Fe}/\text{H}]$, the lower the abundance of metals within in that star. $[\text{Fe}/\text{H}] = 0$ indicates that a star has solar metallicity.

Usually this metallicities are measured by comparison of photometric and spectroscopic measurements from a star. Fraunhofer CaHK lines are a signature of singly ionised calcium being present in the atmosphere of a star. The absorption occurs at 3968.47 for the H line and at 3933.66 for the K line. Often, it is more feasible to look for CaHK absorption

lines rather than the absorption lines associated with iron. Fe absorption lines are usually small and are found across a large range of wavelengths, making them extremely hard to measure without high resolution spectroscopy. This issue is amplified for metal-poor stars that are in the stellar halo (~ 10 kpc away).

CaHK lines can be used to infer stellar metallicity in place of iron, as the abundance of calcium typically traces that of iron in a star. The abundances are similar as they are both synthesised by the r-process during supernovae of massive stars or white dwarfs. The r-process, or rapid process, involves the capturing of neutrons by seed nuclei over a timescale such that the nuclei cannot undergo nuclear decay before being bombarded by another neutron (Arnould et al. 2007). Therefore, the ratio $[\text{Ca}/\text{H}]$ will be reflective of $[\text{Fe}/\text{H}]$. Figure 1 shows the variation of the CaHK absorption profile with $[\text{Fe}/\text{H}]$ for a Sun-like star. While the depth of the lines does not noticeably change, the breadth of the absorption lines increases with increasing $[\text{Fe}/\text{H}]$, thereby making stars look fainter at these wavelengths. As well as singly-ionised calcium, there are numerous other elements present in an atmosphere of a star such as the Sun. This results in many absorption lines spread over a wide range of wavelengths, which can be best observed in the $[\text{Fe}/\text{H}] = 0$ line of Figure 1.

As a consequence, metallicity directly affects the apparent colour of a star. Since metals preferentially absorb light of shorter wavelengths, metal-rich stars appear redder than their metal-poor partners at a fixed surface temperature. This effect is called line blanketing⁵.

2.4 What spectral Type would Population III Survivors Be?

A low mass Population III survivor would have an age of the order of the age of the universe. From the main sequence lifetimes shown in Table 1, it is clear that population III survivors must be G or K type stars. Based on simulations of the primordial halo evolution, it was thought stars with mass greater than $100 M_{\odot}$ were more favourable (e.g. Bromm et al. 2002). It was argued that primordial gas can only perform continued gravitational collapse and fragmentation, and therefore star formation, if the gas can effectively radiate away the gravitational binding energy that is released in this process. This process is only possible at gas cloud masses above $10^6 M_{\odot}$, which under collapse only produces large stars. However, in recent years, as computational capabilities and understanding of fragmentation have improved, Stacy et al. (2016) have provided greater simulation resolution of mini-halos showing protostars form with masses between 0.1 to $1000 M_{\odot}$, mainly due to fragmentation of protostellar discs, therefore suggesting that G and K type stars were feasible in the early Universe. M spectral type stars would form in the early Universe, but would be heavily suppressed. The problem with this simulation is that it only produces protostars, therefore it is assumed that all these protostars would go on to perform nucleosynthesis and the final stellar mass will be much larger.

⁴ <http://astronomy.swin.edu.au/cosmos/P/Population+III>

⁵ <https://iopscience.iop.org/article/10.1086/128651/pdf>

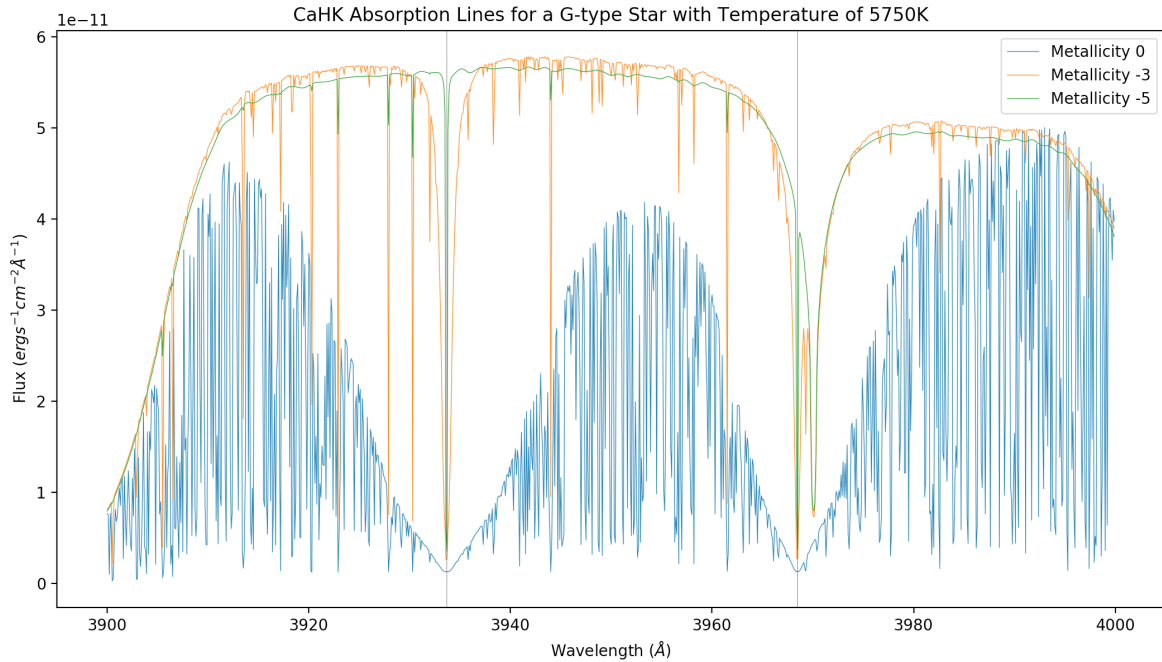


Figure 1. Plot to show the effect of varying $[\text{Fe}/\text{H}]$ on the CaHK lines (at 3968.47 and 3933.66 respectively) on a G type star with temperature 5750K. Note the significant effect of metallicity on the CaHK absorption features, making it a very sensitive $[\text{Fe}/\text{H}]$ indicator.

2.5 Why Search for Metal-poor Stars in the Halo?

The halo of a galaxy is a broad, roughly spherical structure which extends beyond the visible edge of the galaxy. Including dark matter, the halo contains the vast majority of a galaxy's mass and, in the case of the Milky Way, is approximately 100 kpc from the Earth⁶. The location of Population III stars would likely be in globular clusters close to the galactic nucleus, as this appears to be the edge at which Population II stars are observed. However looking towards the galactic nucleus is like looking through fog. In comparison, looking towards the galactic halo bears less contamination of the data set with Population I stars. In addition, stars found in the nucleus have a high chance of being contaminated by metals from stellar winds, and therefore lose their metal-poor status.

Some hypotheses suggest that the formation processes of Globular Clusters (GC) mean Population III are present in GCs, although there have been many theorised postulates based upon GC formation, and not all of them agree on one hypothesis. One such postulate, proposed by [Trenti et al. \(2015\)](#), suggests that mergers of gas-rich, but star free, mini-halos can cause instantaneous compression and form central stellar clusters. These would eventually be stripped of their dark matter envelope and become the GCs with ancient stellar populations that we see today. This postulate seems likely due to fundamental physics it is based upon in this high redshift era. Firstly the actual formation of large spiral galaxies in this period was significantly low, secondly

the merger rate was incredibly high in the early Universe and lastly the high temperature of the CMB ($T > 30\text{K}$) limits the cooling of the gas making it difficult to form stars. Once the Universe cools, and finally allows the formation of larger stellar structures, two types of GCs arise, metal poor and metal rich GCs based on their location of formation. GCs formed inside the radius of the host primary galaxy are generally more metal rich whereas GCs captured from outside the primary galaxy are more metal poor ([Forbes et al. 2018](#)). The position of the ‘beginning’ of the halo can be estimated by finding the distance at which the number of stars in a data set abruptly drops off. Current estimates for the distance of the Milky Way’s stellar halo is at approximately 30 kpc,⁷ to around 200 kpc⁸.

2.6 Background Galaxies

While surveying the sky, and particularly at very low fluxes, number counts become dominated by distant galaxies that may resemble stars. This leads to the need to carefully distinguish between stars and galaxies. Edwin Hubble, in 1929, while measuring distances to galaxies, concluded that the Universe, and any space where objects are not bounded by electromagnetic or gravitational forces, was expanding at a velocity directly proportional to the distance the object is

⁶ <https://www.cfa.harvard.edu/research/oir/milky-way-halo>

⁷ https://imagine.gsfc.nasa.gov/features/cosmic/milkyway_info.html

⁸ <https://ned.ipac.caltech.edu/level5/Ashman2/Ashman3.html>

from us (e.g. Hubble 1929). This is shown by equation 3,

$$\vec{v} \propto \vec{d} \quad \vec{v} = H\vec{d} \quad (3)$$

where v is recessional velocity, d is distance from Earth and H is the Hubble Constant. At large recessional velocities, the redshift, z , must take into account relativistic corrections. When the object travels directly away from the observer, the redshift is given by equation 4 (c is the speed of light in a vacuum).

$$z = \sqrt{\frac{c+v}{c-v}} - 1 \Rightarrow z = \sqrt{\frac{c+Hd}{c-Hd}} - 1 \quad (4)$$

A star within our halo will have $z \approx 0$, although there may be some redshift due to a stars rotation about the galactic centre. Galaxies outside the Local Group will have considerably larger redshifts.

2.7 AB Magnitude System and Colour-Colour Diagrams

AB magnitudes (Oke 1974) are defined as follows,

$$m_{AB} = -2.5 \log_{10} f_{\nu} - 48.60 \quad (5)$$

where m_{AB} is the AB magnitude and f_{ν} is the flux density in units of $\text{erg s}^{-1} \text{cm}^{-2} \text{Hz}^{-1}$. Flux density (defined per unit wavelength, f_{λ}) can be converted into flux density (flux per unit frequency) using equation 6,

$$f_{\nu} = \frac{\lambda^2}{c} f_{\lambda} \quad (6)$$

where c is the speed of light and λ is the wavelength.

Colour-colour diagrams are created using different combinations of magnitudes in different bands as the axis. An example of a colour index, $(g - i)$, where g and i are the magnitudes in the green and the infrared filter respectively. Stars are effectively black bodies, so a colour index is directly related to properties of astronomical objects, such as their intrinsic colour or temperature. Therefore the positioning of data-points on colour-colour diagrams can, for example, indicate the relative metallicities of corresponding stars. Since metal-rich stars appear redder, we can expect their $(g - i)$ indices to be more positive than those of their metal-poor counterparts.

3 DATA AND SAMPLE

3.1 Initial Catalogue

Our dataset used CaHK observations conducted with the MegaPrime/MegaCam on the CFHT (programs 15BC10, 16A038 & 17BO54 PI: David Sobral)⁹, together with masks previously designed by D.Sobral, to produce a CaHK catalogue of sources using SEXTRACTOR. The 2'' diameter aperture used for CaHK magnitudes found 62,652 sources, extending to a depth of $m_{HK} = 26$.

This CaHK catalogue was then combined with broadband COSMOS photometry data (Scoville et al. 2007),

⁹ Information on these programs can be found at: <http://www.cadc-ccda.hia-ihp.nrc-cnrc.gc.ca/en/search/?collection=CFHT&noexec=true>

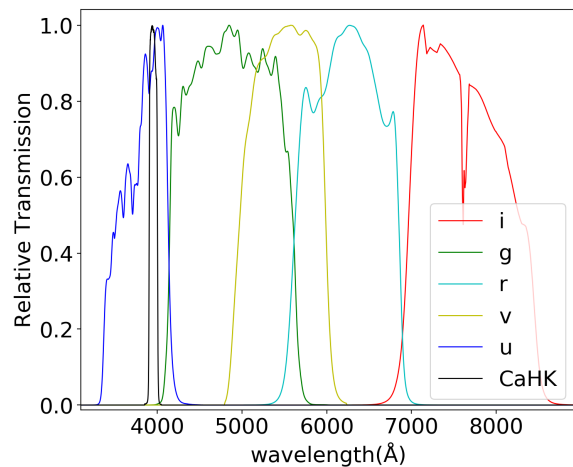


Figure 2. Normalised transmission profiles for various filters used in this study.

Filter	$\Delta\lambda$ (Å)	λ_{eff} (Å)
i	1168.1	7641.3
g	1304.2	4912.8
CaHK	94.2	3953.4
v	972/4	5505.9
r	1092.9	6251.1
u	528.7	3835.2

Table 2. Summary of the bandwidths ($\Delta\lambda$) and effective transmission wavelengths (λ_{eff}) of each filter obtained from the filter profiles.

which added optical and near-infrared magnitudes, such as u, g, r, i, v, j, z and k and their associated errors. The filter profiles of u, g, r, i, v and CaHK are plotted in Figure 2. The bandwidths and effective wavelengths of u, g, r, i, v and CaHK are displayed in Table 2.

A record of the subsequent cuts made to the initial LAMPSS catalogue are shown in Table 3, and a description of how these cuts are made is given in the relevant subsections of §3.

3.2 Magnitude Cuts

In order to mitigate large uncertainties in the metallicity and $(g - i)$ conditions, we excluded sources that are too faint by placing a magnitude limit on several bands. This also removed sources which have undefined magnitudes in certain bands (which appear blank or as 99.9 in the catalogue). The limits used are shown in Table 4. For bands imported from the COSMOS catalogue we used cuts given in Capak et al. (2007). For CaHK magnitudes we simply devised our own magnitude limit, by observing at what magnitude the counts in Figure 3 begin to fall off ($m_{HK} = 26$). By a miscommunication, $m_{HK} = 25.3$ was used for volume calculations (§4.7). However, since limiting at $m_{HK} = 26$ only removes 0.973% of the catalogue and due to time constraints, we decided the incompleteness this created was negligible.

Catalogue Version	Sources	Notes	Described in Section
n/a	2,017,800	Full COSMOS photometry	n/a
0.0	62,652	Merge COSMOS and CaHK data	3.1
1.0	1,930	Magnitude and EGO cuts	3.2/3.3
1.1	1,930	Added internal ID to each source	n/a
1.2	1,930	Added distances to each source	4.6
1.3	1,930	Applied metallicity conditions	4.4

Table 3. Walkthrough of all major catalogue versions, number of sources within each version and notes on cuts made.

i^+	r^+	u^*	V_J	g^+	B_J	m_{HK}
26.2	26.8	26.4	26.6	27.0	27.3	26.0

Table 4. Magnitude cuts performed on our catalogue, all except m_{HK} are given magnitude limits for COSMOS [Capak et al. \(2007\)](#).

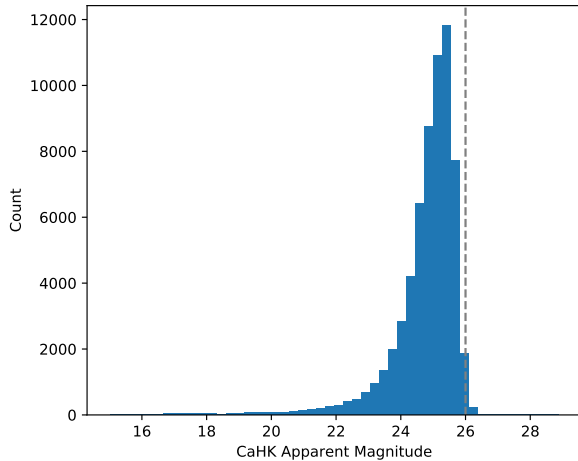


Figure 3. Histogram of CaHK magnitudes of sources through a 3'' diameter aperture. The vertical line shows the magnitude cut applied to the catalogue at $m_{\text{HK}} = 26$, removing 0.973% of the catalogue.

3.3 Star-Galaxy Separation

The primary purpose of the COSMOS survey was to observe galaxies and their evolution over time, as a consequence, the majority of sources in the *LAMPSS* catalogue are Extra-Galactic Objects (EGOs). These EGOs had to be removed before searching for metal-poor stars within our halo.

J and K are two infrared bands between 1.1 to 1.4 μm and 2.0 to 2.4 μm respectively. Sources at a higher redshift have a larger $(J-K)$, than those at smaller redshifts, as such, $(J-K)$ -colour diagrams are an effective way to separate stars and galaxies.

Using TOPCAT subsets, we defined sources within our catalogue with zero spectroscopic redshift ($z_{\text{spec}} = 0$) as stars and sources with $0.1 \leq z \leq 8$ as galaxies. We investigated plots of $(J-K)$ against other colour indices were made in order to determine the cleanest cut, all plots trialled are in Table 3 in Appendix ???. The cleanest cut was

found by plotting $(J-K)$ against $(B-u)$ (see Figure 4), and gave the following criteria for stars:

$$(J-K) < -0.6143(B-u) - 1.6121 \quad (7)$$

$$(B-u) < -0.674 \quad (8)$$

There were two conditions, as the contamination seemed to increase as $(B-u)$ increased as shown in figure 4. Completion and contamination are defined below by equations 9 and 10. The $(J-K)$ against $(B-u)$ criteria returned a contamination of 30% and a completion of 70%.

$$\text{Completion} = \frac{N_{\text{stars kept}}}{N_{\text{stars total}}} \quad (9)$$

$$\text{Contamination} = \frac{N_{\text{galaxies kept}}}{N_{\text{galaxies kept}} + N_{\text{stars kept}}} \quad (10)$$

4 METHODOLOGY

Following our sample reduction, we were left with 1930 sources which we classified as stars. However, since our star-galaxy separation has 30% contamination, it is likely that many of these 1930 sources will be galaxies. Due to time constraints, we could only manually check the nature of sources with low metallicity using *HST* imagery (§4.5). In this section we describe our methods to classify these stars by spectral type and metallicity, as well as calculate distances to the stars.

4.1 Magnitude Calculations

In order to interpret observed magnitudes, we analysed a range of spectra of stars of known temperatures, spectral types and metallicities. This was necessary to compute magnitudes in a range of filters and construct a colour diagram. The effect of temperature and metallicity could then be seen through carefully choosing appropriate colour combinations to be plotted on the y- and x- axes. Stellar spectra, obtained from the POLLUX database¹⁰, and filter profiles of different filters of the MegaCam/MegaPrime on the CFHT were interpolated and re-expressed as a continuous function of wavelength in a PYTHON script. An example of an interpolated spectrum can be found in Figure 5.

The filter profiles, shown in Figure 2, were normalised, such that they consisted of relative light transmission, ranging between 0 and 1, as a function of wavelength. The band

¹⁰ <http://npollux.lupm.univ-montp2.fr/>

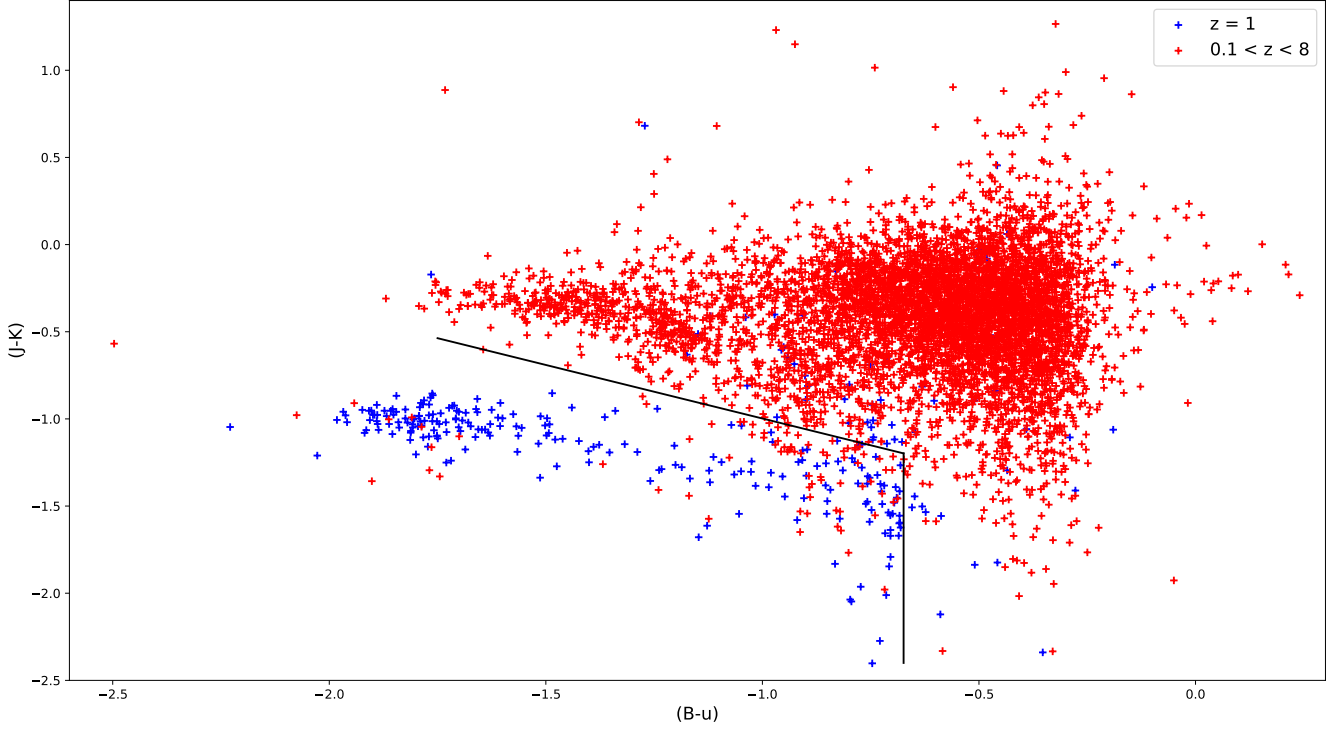


Figure 4. Color-Color plot of $(J-K)$ against $(B-u)$ for the initial LAMPSS catalogue. EGOs are separated from stars by spectroscopic redshift (stars: blue, galaxies: red). The black line shows our chosen conditions to remove EGOs (equations 7 and 8)

width, $\Delta\lambda$, of each filter was found by integrating the profiles with respect to wavelength using the trapezoidal rule. The effective transmission wavelength of each filter was computed using a weighted mean method outlined in the Appendix in §???. The band widths and effective transmission wavelengths of each filter used can be found in Table 2.

We start by normalising the flux densities, such that all stars appeared to be located at 10 parsecs. To achieve this, firstly, the Stefan-Boltzmann Law, given by,

$$L = 4\pi\sigma R^2 T^4 \quad (11)$$

where L = absolute luminosities, σ = Boltzmann constant, R = Radius of star and T = Temperature of star, was employed to calculate the luminosity given the temperature and radius. The range of radii and temperatures used for each spectral type are shown in Table 5. Subsequently, the interpolated stellar spectra were integrated with respect to the wavelength (in angstroms, \AA) to obtain the total flux (an example spectrum can be found in Figure 5). The luminosity, L , at 10 pc was found using the following equation:

$$L = 4\pi d^2 F \quad (12)$$

Where F is the total flux in units of $\text{erg s}^{-1} \text{cm}^{-2} \text{Hz}^{-1}$ and d is $3.086 \times 10^{19} \text{cm}$ (10pc). The convolved flux, $F_{\text{conv},i}$, as a function of wavelength was computed using the following formula:

$$F_{\text{conv},i} = F_i I_i R \quad (13)$$

where F is the flux from the spectrum, I is the rela-

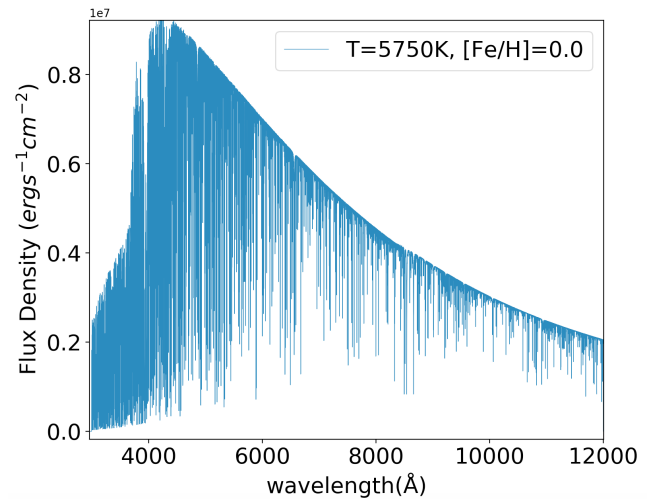


Figure 5. Spectrum of a G-type star of temperature $T_{\text{eff}} = 5750 \text{ K}$ and $[\text{Fe}/\text{H}] = 0.0$

tive transmission from the filter profile, i indicates the i th data-point and R is a ratio of the luminosity obtained via Stefan-Boltzmann law, L_{typical} , and the luminosity at 10 pc calculated using Equation 12. Multiplication by the ratio, R , ensured that integrating the convolved flux would result in the total flux in each filter as seen from 10 pc. This was repeated for each filter. An example of a Solar-like spectrum convolved through the i , g , r , v , u and $CaHK$ filters is presented in Figure 6.

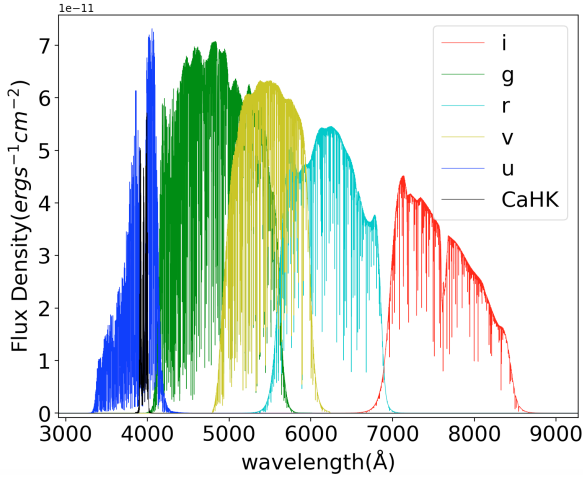


Figure 6. Solar-like spectrum from Figure 5 convolved through the *i*, *g*, *r*, *v*, *u* and *CaHK* filters.

Subsequently, the convolved spectra were integrated using trapezoidal rule to obtain the total flux seen through each filter, F_{eff} . The effective flux was then converted into flux density per unit wavelength, f_{λ} , as follows:

$$f_{\lambda} = \frac{F_{\text{eff}}}{\Delta\lambda} \quad (14)$$

where $\Delta\lambda$ is the previously calculated filter band width from Table 2. This was converted into flux density per unit frequency, f_{ν} , using Equation 6 with λ being the effective transmission wavelength, λ_{eff} , obtained using Equation ???. Knowing the flux density, f_{ν} , the AB magnitudes in each filter were computed using equation 5.

4.2 Estimating Stellar Radii

While the temperatures and metallicities of each star were known, the radii values were assumed to be the average radii for each spectral class and the uncertainties were chosen such that the smallest and largest stars of each spectral type were encompassed by the errors. In order to implement this, a Gaussian distribution of stellar radii was generated and a random radius value, within 3 standard deviations of the average radius for each spectral type, was picked to perform the luminosity calculation. The summary of radii used is presented below in Table 5.

For convenience, and because we do not expect O type Population II stars, the upper size limit for this spectral type was set to be $R = 26.6R_{\odot}$. Similarly, since M type Population III stars are not expected to be observed the lowest size limit for M type stars was set to be $R = 0.3R_{\odot}$. The process of computing AB magnitudes as described in Subsection 4.1 was repeated for a 1000 iterations for each stellar spectrum, each time with a different, randomly generated radius. This was to ensure that that magnitude predictions are as accurate as possible, despite not having access to any information about the stars' sizes and distances. After each iteration the radii, luminosities and magnitudes in each filter were stored in separate lists. The final values and uncertainties of those quantities were computed by calculating the average and the

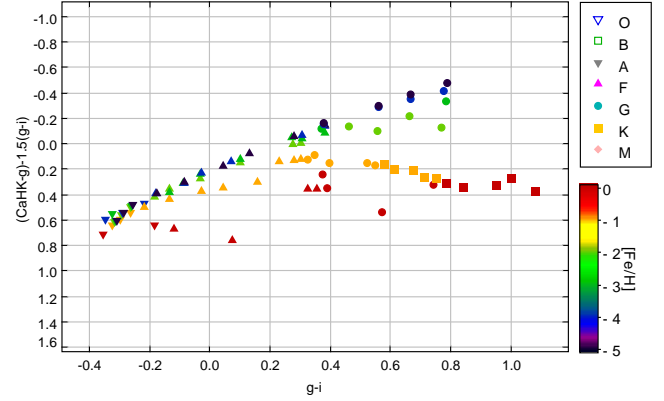


Figure 7. Variation of the stars' colours with metallicity. The shape of data-points represents the spectral type, whereas the colour indicates the metallicity. The hottest stars are shifted towards the negative colour indices along both axes. Here we concentrate on A, F, G and K type stars, showing the variation of stars' colour with metallicity. The shape of data-points represents the spectral type, whereas the colour indicates the metallicity. The hottest stars are shifted towards the negative colour indices along both axes.

standard deviation of the lists. The results were stored in a Table to be later used in TOPCAT to produce magnitude graphs.

4.3 Colour-Colour Predictions

In order to be able to distinguish between spectral types the $(g-i)$ index range for each spectral class was estimated using Figure 7. This was necessary as it allowed the star volume density per spectral type calculations at a later time in the project. The summary of the $(g-i)$ ranges is presented in Table 6.

Figure 7 shows a colour plot of all stars used for the theoretical predictions. In order to estimate metallicities for our stars, the y-axis values were chosen to be $(HK-g) - 1.5(g-i)$ colour index and the x-axis values were $(g-i)$. This was in agreement with the colour combinations used in the *Pristine survey* (Starkenburger et al. 2017) and this combination of magnitudes resulted in the largest spread of data-points corresponding to stars of metallicities $[\text{Fe}/\text{H}] \leq -3.0$.

Figure 7 presents a close-up concentrating on F, G and K type stars and providing a clearer picture of how metallicity affects the intrinsic colour. The more negative the $(g-i)$ index (x-axis) the hotter the star (the y-axis is inverted). Generally, stars of lower metal content tend to shift towards more negative values along the y-axis within the same spectral class. This is in agreement with theory, indicating metal poor stars appear bluer than their metal rich spectral type companions.

4.4 Metallicity Conditions

The magnitude predictions from §4.1 allowed us to derive metallicity conditions to determine the metallicities of the stars in the *LAMPSS*. This was done by using NUMPY'S

Spectral Type	Radius (R_{\odot})	Temperature Range (K)	Metallicity Range
O	16.600 ± 10.000	$> 30,000$	$[\text{Fe}/\text{H}] = 0.0$
B	4.200 ± 2.400	$10,000 - 30,000$	$-1.0 \leq [\text{Fe}/\text{H}] \leq 0.0$
A	1.600 ± 0.200	$7,500 - 10,000$	$-3.0 \leq [\text{Fe}/\text{H}] \leq 0.0$
F	1.275 ± 0.125	$6,000 - 7,500$	$-5.0 \leq [\text{Fe}/\text{H}] \leq 0.0$
G	1.005 ± 0.095	$5,000 - 6,000$	$-5.0 \leq [\text{Fe}/\text{H}] \leq 0.0$
K	0.830 ± 0.130	$3,600 - 5,000$	$-1.0 \leq [\text{Fe}/\text{H}] \leq 0.0$
M	0.500 ± 0.200	$< 3,600$	$[\text{Fe}/\text{H}] = 0.0$

Table 5. The summary of radii and temperatures used for magnitude calculations and ranges of metallicities obtained from the Pollux database for each spectral type.

Spectral Type	$g-i$ Condition
O	< -0.50
B	-0.5 to -0.40
A	-0.40 to -0.25
F	-0.25 to 0.30
G	0.30 to 0.80
K	0.80 to 2.40
M	> 2.40

Table 6. The $g-i$ conditions used to separate dataset into spectral types.

polyfit function, fitting each line to the POLLUX data points for each metallicity in terms of $(g-i)$. When using different degrees of the fit, it was found that that the POLLUX data points at $(g-i) \approx -1$ and $(g-i) \gtrsim 1.5$ greatly affected the fitting of the curves. When these points were removed from consideration, each fit used degree 2 in the polyfit function. In order to then create conditions for each metallicity, the intermediate lines of the fitted lines were found such that the fitted line in between two adjacent intermediate lines would be the metallicity contained in the two intermediate lines. Figure 8 shows the fitted lines in colour and the intermediate lines in black.

Removing points with $(g-i) \lesssim -1$ and $(g-i) \gtrsim 1.5$ will not affect our predictions for G type stars because for G type stars in the LAMPSS catalogue $0.3 \lesssim (g-i) \lesssim 0.8$. However our $(g-i)$ range for K type stars lies partly outside of the $(g-i)$ range where our metallicity conditions are valid.

The equations of these lines that allowed the metallicity conditions to be created are shown in table ?? . It must be noted that the conditions above metallicity 0 and below metallicity -5 have not been created, meaning any star that falls in the conditions for 0 metallicity may be, for example, a star with metallicity +1. This is the same for stars in the conditions for metallicity -5, which may have lower metallicity (although this is extremely unlikely). Furthermore, the presence of 'hard borders' creates limitations because the metallicity of each star is only known to be within a region and does not have a precise value.

4.5 Visual Inspection of the Most Metal-Poor Candidates

Table 7 shows the number of stars of each metallicity found after applying the metallicity cuts. The number of star with $[\text{Fe}/\text{H}] = -3$, $[\text{Fe}/\text{H}] = -4$, $[\text{Fe}/\text{H}] = -5$ appeared to be unexpectedly large. This was due to the fact that our star sample was contaminated with galaxies (30% contamination), since it was impossible to remove all galaxies in the single

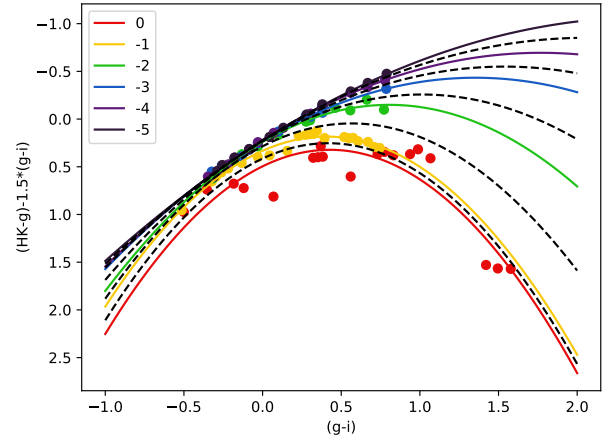


Figure 8. Plot showing the conditions created for each metallicity over the theoretical POLLUX data. The midlines showing the boundaries for each metallicity are shown in black. Metallicity conditions for each $[\text{Fe}/\text{H}]$ step are listed in Table ?? .

$[\text{Fe}/\text{H}]$	Number
0	1145
-1	352
-2	259
-3	61
-4	21
-5	92

Table 7. Summary of number of object of each metallicity found before the visual checks with *HST* images were carried out. This table includes all spectral types.

cut described in section 3.3. It was expected that a large number of objects included in Table 7 were galaxies, thus it was decided that it was necessary to visually check images of those objects and remove any unwanted sources using *HST* images.

Images taken by the Hubble Space Telescope (*HST*) were downloaded and any objects which were not point-like were rejected. Only objects with $[\text{Fe}/\text{H}] = -3$, $[\text{Fe}/\text{H}] = -4$ and $[\text{Fe}/\text{H}] = -5$ were checked, as stars of higher metallicities were not the primary focus of this project. An example of a source which was removed (a galaxy) is shown in Figure 9 (left). Sources of larger metal abundance were not considered. The results are summarised in Table 7.

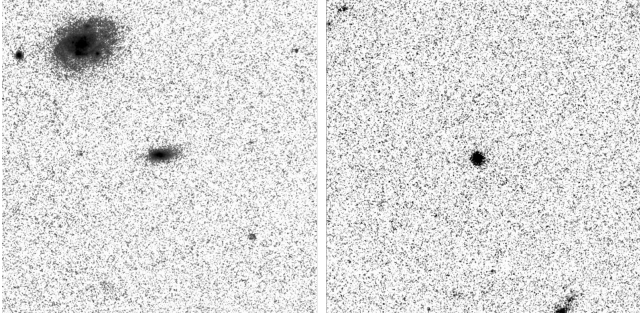


Figure 9. Side by side comparison of two *HST* frames centered on catalogue objects. **Left:** Frame centered on a galaxy – evident by elongated shape and diffuse edges (LAMPSS_944). **Right:** Frame centered on a star - this has a circular, point-like profile (LAMPSS_1254).

4.6 Distance Calculations

After applying the galaxy cuts and removing any sources that are too faint, or have unknown magnitudes, in the filters of interest, namely *i*, *g*, *r*, *v*, *u* and CaHK, distances to all the remaining objects were calculated. This allowed the qualitative assessment of volume density per spectral type and volume density per metallicity. The distance was obtained through the distance modulus equation:

$$\log_{10}(d/pc) = \frac{m - M + 5}{5} \quad (15)$$

Where *d* is the distance in pc, *m* is the apparent magnitude and *M* is the absolute magnitude. The distance was calculated 5 times, each time using magnitudes in a different filter. The CaHK band was not used for this step. Since it is sensitive to metallicity, the magnitudes and therefore distances are unreliable. The apparent magnitudes and their corresponding errors were extracted from the catalogue. The absolute magnitude in each filter was determined using theoretical data from subsection 4.1. Firstly, the script sorted the data into spectral types based on temperature given in Table 5 and calculated an average AB magnitude in each filter for each spectral type. This average value had an error equal to the standard deviation of each point where the standard deviation was given by:

$$\sigma_{SD} = \left(\frac{\sum_i^N (M_i - \bar{M})^2}{N^2 - N} \right)^{\frac{1}{2}} \quad (16)$$

where *N* was number of values, \bar{M} was the mean absolute magnitude and *M_i* was the *ith* magnitude used for the average calculation. Each data point also had an associated error with its band magnitude which was incorporated into this standard deviation. The combined error was calculated using:

$$\sigma_{CB} = \frac{1}{N} \left(\sum_j \sigma_j^2 \right)^{\frac{1}{2}} \quad (17)$$

where σ_j is the *jth* error in a particular filter. Therefore the total error of each average is given by:

$$\sigma = (\sigma_{SD}^2 + \sigma_{CB}^2)^{\frac{1}{2}} \quad (18)$$

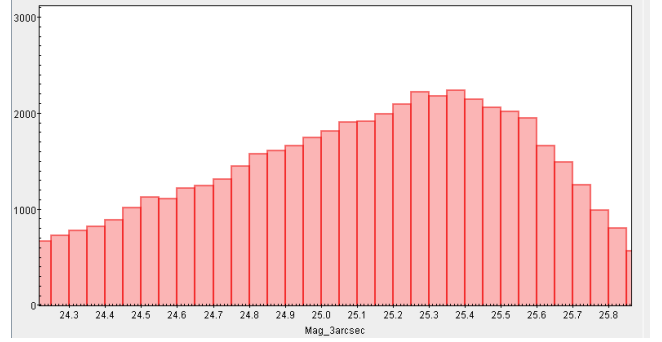


Figure 10. HK apparent magnitude (3'' aperture) histogram for the entire LAMPSS catalogue. Counts begin to fall off at $m_{HK} \approx 25.3$, so this was used as the maximum magnitude for volume calculations.

Table ?? shows the absolute magnitudes used to calculate the distances.

Calculating the (*g* – *i*) index using the extracted apparent magnitudes, and therefore determining the spectral type, ensured the code was able to pick out an appropriate absolute magnitude. A loop was used to calculate the (*g* – *i*) index, choose an absolute and an apparent magnitude and calculate the distance using equation 15. The uncertainties were propagated using:

$$\sigma_{d,j} = 10 \ln 10 \sqrt{a + b} \quad (19)$$

where

$$a = \left(10^{-\frac{M_j}{5}} 2^{\frac{m_j}{5}} 5^{\frac{m_j}{5} - 1} \right)^2 \sigma_{m_j}^2 \quad (20)$$

$$b = \left(10^{\frac{m_j}{5}} 2^{-\frac{M_j}{5}} 5^{-\frac{M_j}{5} - 1} \right)^2 \sigma_{M_j}^2 \quad (21)$$

Here, σ_d is the distance uncertainty, *M* refers to the absolute AB magnitude, *m* represents the apparent AB magnitude and the subscript *j* refers to the *jth* filter. This process was repeated 5 times, each corresponding to a different filter. The final distance value was the mean of those 5 computations, whereas the final uncertainty was obtained using the standard deviation formula (Equation 16).

4.7 Calculating Volume

Volumes for each spectral type of star were calculated by approximating our region of sky as a section of a sphere. This was a valid approach, as the solid angle subtended by the spherical section was found to be only 1.010deg² ($\approx 41253\text{deg}^2$ in a sphere) by studying the RA and Dec of our un-cut catalogue. The radii of the sections was calculated by using HK magnitudes of stars of solar metallicity obtained from POLLUX data by methods described in section 4.1 and the distance modulus (Equation 15). The maximum m_{HK} was assumed to be 25.3 by judging where the counts of Figure 10 began to fall off. The results of the volume calculations can be seen in Table 8, B stars were not included as none were present in the catalogue after applying the star-galaxy separation criteria (§3.3) and the (*g* – *i*) conditions (§4.3).

Spectral Type	m_{HK}	d_{max} [kpc]	V [pc ³]
O	4.512	143.7	3.043×10^{11}
A	4.815	125.0	2.003×10^{11}
F	5.407	95.19	8.846×10^{10}
G	6.186	66.49	3.105×10^{10}
K	10.299	10.00	1.026×10^8
M	10.806	7.921	5.097×10^6

Table 8. Absolute HK magnitudes (m_{HK}) for stars of solar metallicity at the central temperature of each spectral type, obtained from POLLUX data. Maximum distance, and volume for each spectral type are also given. B stars are disregarded as we found none within our catalogue.

Spectral Type	Number
O	0
B	0
A	2
F	131
G	1064
K	575
M	0

Table 9. The finalised number of stars of each spectral type remaining after applying the galaxy cuts (using the $J - K$ magnitude and Hubble and removing the stars with $[\text{Fe}/\text{H}] > -3.0$.

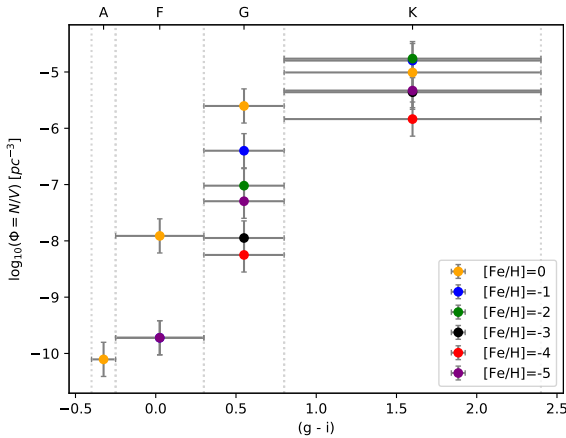


Figure 11. The number density of each spectral type per unit volume per metallicity in the Halo. The density increases with $(g - i)$ and lower metallicity stars are only G and K type stars.

5 RESULTS

5.1 Quantitative Analysis

After applying a variety of cuts described in §4 the spectral type of all the remaining stars was determined by calculating the $(g - i)$ indices. The number of stars per spectral type can be found in Table 9.

Using the maximum distances for stars of different spectral type presented in Table 8 and the area of the field of view which was calculated to be 1.010deg^2 , a graph showing the number density per spectral type was plotted. This can be found in Figure 11.

Table 9 shows that of the stars found, a significant majority of the stars identified were G-type stars, with the next

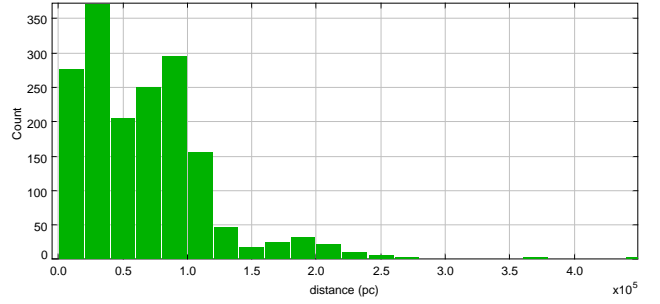


Figure 12. Histogram presenting the number of stars per distance interval. This shows the halo limit where the number of stars drops off.

largest set being K-type stars, F-type stars and just two A-type stars. There were no stars identified that were of spectral types O, B or M. These values of each spectral type should be expected as G and K type stars are two of the most common spectral types due to having such long lifetimes and COSMOS does not track star-forming regions where O and B type stars are formed, hence none of them being identified. The lack of M-type stars can be explained by the fact they are the dimmest, thus hard to detect at large distances. This agrees with our theory as we expected most of the stars to be G type, and a lesser amount to be K type. The number of F types was surprising seeing as they should only live 3-8 Gyrs, which is less than the lifetime of the Universe. This implies these stars must have been created in a metal-poor region of the galaxy between 3-8 Gyrs ago, and then moved out into the halo due gravitational interactions.

Figure 14 shows a 3D positional plot of the LAMPSS catalogue stars. Hotter stars, A- and F-types for our sample, can be observed at much further distances than their cooler partners due to their higher luminosities.

5.2 Distance to Halo

Since the project focuses on metal-poor stars in the halo, it is important to have an estimate of where the halo is located. The plot of the distribution of distances, which can be found in Figure 12, shows there is a drop off in the number of stars at a distance of approximately 120 kpc. This gives an approximate distance of the halo because most stars within a galaxy are in the disc and the bulge, with relatively few in the halo. This value fits nicely within previous studies to estimate the distance to the edge of the halo of 100 – 200 kpc (Battaglia et al. (2005)). Of course, the stars stretch beyond 120 kpc, however the number of them past this value is significantly reduced.

5.3 Metal-Poor Candidates

Having manually checked the images of the $[\text{Fe}/\text{H}] = -3$, -4 and -5 metallicity candidates, the number of stars per metallicity was significantly reduced. The finalised number of candidates of each metallicity per spectral type is shown in Table 10.

When the conditions for each metallicity (see Table

Metallicity	Number of Stars in Spectral Type				
	G	K	A	F	Total
0	886	128	2	129	1145
-1	142	208	0	2	352
-2	34	225	0	0	259
-3	1	14	0	0	15
-4	0	0	0	0	0
-5	1	0	0	0	1

Table 10. The different numbers of spectral types at different metallicities found after removing galaxies using Hubble images.

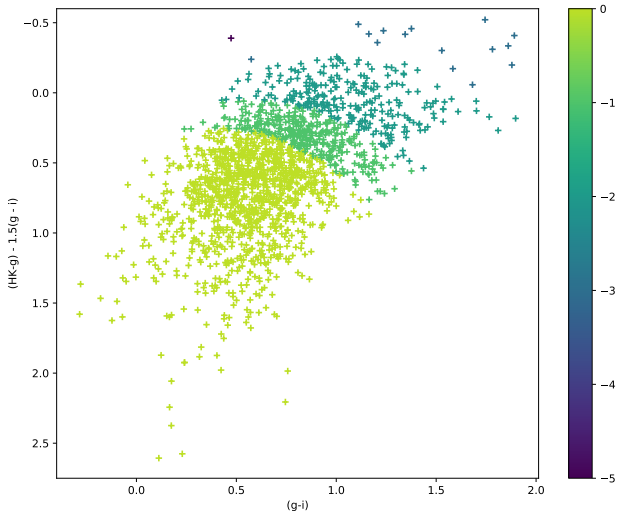


Figure 13. Metallicity plot of finalised catalogue with $(g-i)$ and $((HK-g) - 1.5(g-i))$ colour indices. Metallicity conditions have been applied and for objects with $[Fe/H] \leq -3.0$ galaxies have been visually checked and separated from the catalogue.

??) were applied to the reduced *LAMPSS* catalogue, as expected, the majority of the stars are defined as zero metallicity stars, with a decreasing number of stars as $[Fe/H]$ decreases (see Figure 13). As explained in section 2.1, this is because most stars in the present age formed from an ISM with heavier metals than hydrogen and helium.

Only G and K type stars were found to have $[Fe/H] \leq -3.0$. The colour-colour metallicity diagram for G type stars is shown in Figure 13, while a similar plot for K type stars is shown in Figure ???. A detailed summary of stars surviving those metallicity cuts is shown in Table 11.

While the large number of stars with $[Fe/H] \leq -3$ is surprising as it would appear to contradict the assumption that most metal-poor stars will most likely be G-type stars, it is crucial to emphasise that we are uncertain about the metallicities of all candidates classified as K-type. Since theoretical spectral data obtained contained no K-type stars of metallicity lower than $[Fe/H] = 0$ it cannot be confirmed with any degree of confidence that these particular sources are metal-poor. When fitting the metallicity criteria shown in Figure 8, the $[Fe/H] = -3.0$ curve in the K region ($0.8 \leq (g-i) \leq 2.40$) was an extrapolation of data-points of all preceding spectral types. Moreover there is unusual positioning of the K and M data points, which does not appear to follow a pattern which the other spectral types do. The points corresponding to different metallicities tend to shift towards more posi-

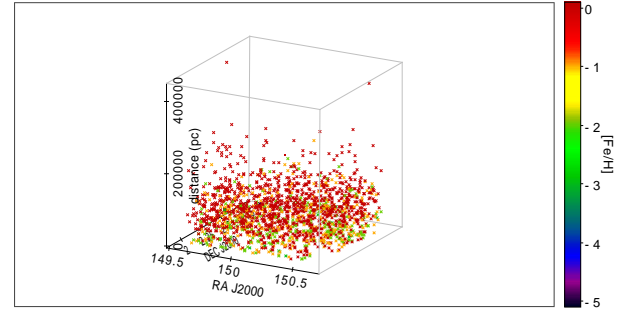


Figure 14. Distance plot showing the stars in the *LAMPSS* catalogue after magnitude and galaxy cuts. The auxiliary axis represents the metallicity.

tive values along the x-axis and more negative values along y-axis as star temperature decreases. However, in the K region at $(g-i) \approx 1$ this is not the case. Here, the y-axis values start increasing, reaching a maximum of $((HK-g) - 1.5(g-i))$ at $(g-i) \approx 1.8$ (it is important to remember the y-axis is inverted), before starting to drop again and steadily decreasing through the M region. This is most likely due to a suddenly increasing flux density in the i -band for the coolest stars as well as the presence of molecules causing molecule absorption lines in the spectra of the M-type stars. Hence, it cannot be ascertained where on the $((HK-g) - 1.5(g-i))$ vs. $(g-i)$ colour-colour plot metal-poor K-type candidates would appear, which reduces the number of candidates with $[Fe/H] = -3.0$ to just one (LAMPSS_1586).

The most-metal poor candidate, LAMPSS_1229 (Shown in Figure 15), had a $(g-i)$ index of 0.4736 meaning it was classified as a G-type. Having produced reliable metallicity curves in the G region due to the large number of theoretical data-points it was agreed that this is the most promising metal poor candidate. The distances to LAMPSS_1229 and LAMPSS_1586 were computed to be 78210.7 ± 9368.5 pc and 118348.3 ± 20978.1 pc with an estimated lifetime of 8.29 ± 1.43 Gyrs and 10.86 ± 2.87 Gyrs respectively putting them in the halo region of the Milky-Way.

It is important to notice that it was realised that the CaHK filter profile was not normalised before calculating the magnitudes - instead its peak transmission was at ≈ 0.9 . The effect of this was checked by carrying out the normalisation and re-calculating the CaHK magnitudes from our theoretical spectra. It was found that magnitudes agreed to 2 decimal places, thus it was not necessary to re-plot the metallicity criteria as the effect was negligible. Furthermore, since the CaHK filter was not normalised to 1, the fluxes

5.4 Metallicity Distribution Function (MDF) of the Halo

To investigate the metallicities of stars in the halo, a metallicity distribution function of the halo has been produced, which can be found in figure 16. Since we are concerned with stars located towards the halo, the minimum distance threshold for this histogram was set at being at a distance greater than 78 kpc, so as to include the singular -5 metallicity star identified (which is at a distance of 78.2 kpc). Due to

ID	[Fe/H]	(g-i)	Spectral Type	Distance (kpc)	RA (J2000)	DEC (J2000)	Lifetime (Gyrs)
LAMPSS_1229	-5	0.4736	G	78±9	149.90224	2.327138	8.29 ± 1.43
LAMPSS_1875	-3	1.3762	K	32±8	150.6464	2.295457	104.99 ± 38.42
LAMPSS_1671	-3	1.8790	K	12±7	149.7748	2.0275638	189.45 ± 168.81
LAMPSS_1586	-3	0.5746	G	118±21	149.90584	1.8717754	10.86 ± 2.87
LAMPSS_1503	-3	1.1630	K	23±6	150.09969	1.890762	80.38 ± 30.80
LAMPSS_1457	-3	1.3449	K	26±7	150.18236	1.9493028	116.32 ± 43.88
LAMPSS_1417	-3	1.8608	K	20±10	150.29182	1.9552598	192.88 ± 158.51
LAMPSS_1373	-3	1.2362	K	20±5	150.40768	1.8676664	92.88 ± 32.19
LAMPSS_1254	-3	1.5835	K	22±11	149.73572	2.1850543	162.76 ± 118.50
LAMPSS_1111	-3	1.1107	K	35±12	150.05904	2.295457	67.87 ± 34.36
LAMPSS_1004	-3	1.8913	K	18±9	150.3845	2.2432206	171.97 ± 122.68
LAMPSS_627	-3	1.2060	K	27±9	150.36208	2.5158165	108.13 ± 52.31
LAMPSS_392	-3	1.6818	K	20±10	149.87767	2.78925	172.81 ± 123.55
LAMPSS_260	-3	1.7448	K	15±4	150.13509	2.6929514	129.87 ± 52.52
LAMPSS_239	-3	1.5282	K	20±10	150.19594	2.824687	130.72 ± 79.47
LAMPSS_56	-3	1.7817	K	22±12	150.5649	2.766089	187.93 ± 147.01

Table 11. Metallicities estimated using metallicity criteria summarised in Table ?? and spectral types of our candidates deduced through calculating the (g – i) index and comparing it to the predictions summarised in Table 6.

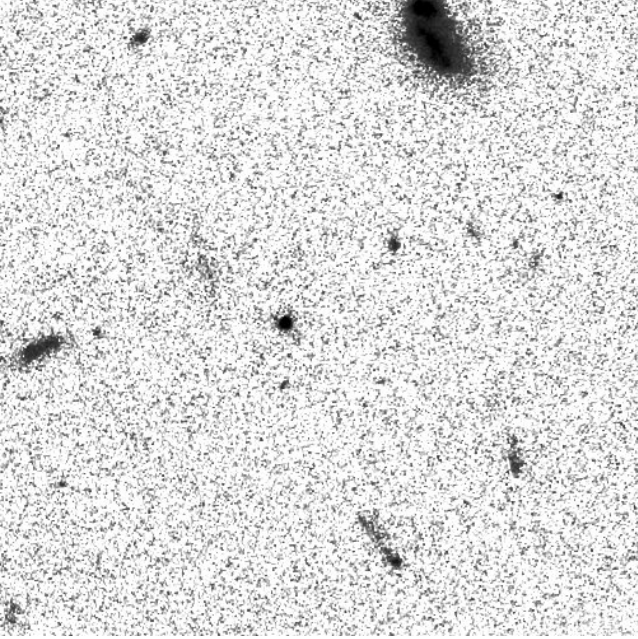


Figure 15. HST image of object LAMPSS_1229

the large number of higher metallicity stars, this star does feature on the histogram.

6 DISCUSSION

6.1 Number of Metal-Poor Stars in Halo

Using the value of 78 kpc as the starting point of the halo (at which the disc is not included and the halo dominates) and 144 kpc as the edge of the halo (which fits with the value of 130 kpc from Battaglia et al. (2005)), an estimate of the volume of the halo of the Milky Way was found, and hence the fraction of this that has been surveyed for the data. With this fraction known, and the known number of metal-poor candidates that came out of the this study, an estimate of

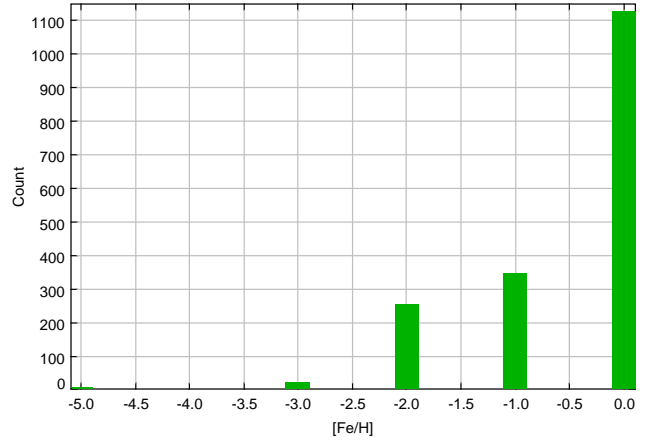


Figure 16. Distribution of stellar metallicities in the Milky-Way halo. It is clear as the number of stars decreases with decreasing metallicity, which is in agreement with the theory.

the total number of metal-poor stars found in the estimated halo. It was found that $\approx 613,000$ stars with $[\text{Fe}/\text{H}] < -3$ and ≈ 40800 stars with $[\text{Fe}/\text{H}] < -5$. These numbers are considerably lower than those presented on M. Magg et al. (2019), this is likely because there is a significant amount of extrapolation used in reaching these estimates so the error involved will be large.

6.2 Halo MDF Compared with Data from HK Survey

A previously produced metallicity distribution function (MDF) of the halo of the Milky Way using data from the HK Survey (Beers & Christlieb 2005) can be used as comparison to the LAMPSS MDF (Figure ??). It is noted that the area surveyed for this distribution is much greater ($\approx 6000 \text{ deg}^2$ vs $\approx 1 \text{ deg}^2$), however the HK survey only probes to a magnitude of ≈ 15.5 compared to ≈ 26 meaning the data used for this report extends to a much deeper field of view.

Even with these dissimilarities, a comparison of the

LAMPSS MDF to the Beers MDF shows that, as expected, the majority of stars have Solar-like, or close to Solar-like metallicities. Beers' MDF shows a peak in metallicity at ≈ -0.5 , whereas for the *LAMPSS* MDF the peak is centred around metallicity of zero, however since the *LAMPSS* cuts are produced in increments of one, it is not possible to determine if a peak would appear around a half-integer value. Moreover, Figure ?? appears to have another peak around ≈ -2.2 , which does not appear in the *LAMPSS* MDF. This is also due to the fact that the methods used to estimate metallicities in this project meant it was only possible to approximate the metallicities as integer values. A more complex method of computing metallicities would be necessary to quantitatively compare both MDFs. Nevertheless, the general trends of both MDFs agree - as metallicity decreases so does the number of stars in agreement with the assumption that metal-rich stars are more abundant in the Universe today.

6.3 Pristine

The Pristine survey (Starkenburg et al. 2017) uses a very similar method to this project, by using Ca HK lines with the wide-field imager MegaCam on the CFHT to search for $[\text{Fe}/\text{H}] = -0.5$ down to the extremely metal-poor $[\text{Fe}/\text{H}] < -3.0$ stars in an area of over 1000 deg^2 of the galactic halo (with an accuracy of 0.2 metallicity). They had a success rate of 24% of selected and filtered stars being $[\text{Fe}/\text{H}] < -3.0$, and 85% of the remaining candidates still being reasonably metal poor at $[\text{Fe}/\text{H}] < -2.0$, from a total of initially 17500 stars, that were filtered down to a total of 7673 stars. In comparison with the results obtained in this project in which 15 stars were determined to have a metallicity of $[\text{Fe}/\text{H}] \approx -3$, which is approximately 0.84% of our filtered stars, it can be seen that the surveys are in support of each other in the discovery of potential EMP candidates. Whilst the *LAMPSS* survey only swept an area of 1 deg^2 it was still deduced that a reasonably significant amount of the determined stars would fall in the metal-poor category. However Pristine was able to deduce which potential candidates were white dwarfs, as white dwarfs typically show no Ca absorption features they are a potential source of contamination in the metal-poor samples, unlike the *LAMPSS* catalogue in which we were unable to determine the difference of white dwarfs and variable stars from the filtered samples, causing a potential contamination error.

6.4 Comparison to WARP (Jenkins et al. 2019)

WARP (We Are Really Poor; Jenkins et al. 2019), have a somewhat parallel effort to ours to find Population III candidates, however they use data from the Isaac Newton Telescope (INT).

Final *WARP* and *LAMPSS* catalogues were matched by the RA and Dec. of the objects, detecting a total of 42 astronomical sources. Figure 17 shows the linear correlation between metallicities computed by independently by *WARP* and *LAMPSS* for those objects and it indicates that, on average, metallicity estimates from both groups agree. The maximum allowed error in arcseconds was set to 1 arcsecond. This plot was greatly limited by a number of factors.

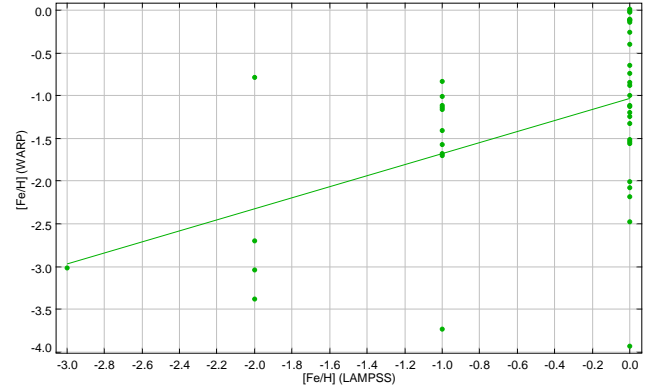


Figure 17. WARP (Jenkins et al. 2019) metallicities vs. *LAMPSS* metallicities of final catalogue objects.

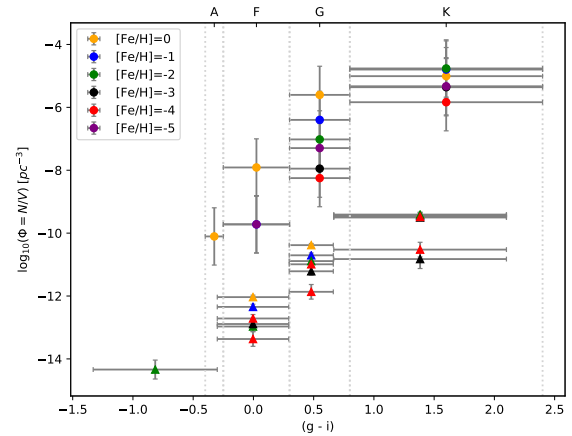


Figure 18. *LAMPSS* number densities plotted with *WARP* values (shown as \blacktriangle ; Jenkins et al. 2019). *WARP* data gives smaller densities over all spectral types.

Firstly, while *WARP* implemented a method of calculating a metallicity that included decimal error estimations (see Jenkins et al. 2019), our process only allowed the estimation of $[\text{Fe}/\text{H}]$ to an integer precision. Furthermore, both groups did not carry out visual checks of images for metal-rich stars thus rejecting galaxies. A result of this can be seen in the large spread of data-points, particularly around $[\text{Fe}/\text{H}] = 0.0$ and $[\text{Fe}/\text{H}] = -1.0$ (*LAMPSS*).

6.5 Calcium Abundances

For these results, we have assumed that the Ca II lines and therefore calcium abundances trace those of iron, as a means to produce the metallicity of a star. However studies have shown that over large metallicities differences, the homogeneity of Ca II to iron does not remain. Vázquez et al. (2015) calibrated their $[\text{Fe}/\text{H}]$ using K giant stars in the Galactic halo, finding that by adding a second-order correction could get a linear correlation over $-2.3 < [\text{Fe}/\text{H}] < 0.7$, however without, a range of $-1 < [\text{Fe}/\text{H}] < 0.7$. Carrera et al. (2007) also recorded similar results, finding linear cor-

relation over $-2.2 < [\text{Fe}/\text{H}] < 0.47$, using almost 500 stars in 29 galactic open and globular clusters. The only concern is that we did not use the Ca II triplet, we used the CaHK lines, but seeing as both lines are from singly ionized calcium, these results should still apply. As in our data (§4.3), we changed the metallicity data into g-i magnitudes as metals affect g-i values. Therefore there might be a range where cannot be certain of the metallicity when using CaHK. However both these studies were performed on giant stars, whereas we are looking at main sequence stars. When a star of mass in the range $0.8M_{\odot} < M < 5M_{\odot}$ exhausts its core of Hydrogen, hydrogen shell burning occurs around the inert core. Once the star reaches the RGB (Red Giant Branch), the star begins to ‘dredge’ up its fusion products. This happens as the convective zone begins to expand further down into the star, bringing down fusion materials and take up fusion products. If the dredge up brings up fusion products then the metallicity of the giant will increase, or depending on the makeup of the star, might also reduce it. This may explain the curve in Ca observed in (Vásquez et al. 2015) and (Carrera et al. 2007). Main sequence stars are more consistent than this, therefore this may not apply to our stars.

7 CONCLUSION AND FUTURE WORK

We present the results from the Lancaster Astrophysics Metal Poor Star Search (*LAMPSS*) to identify the most metal-poor stars towards the galactic halo using the metallicity-sensitive CaHK lines. The project was conducted using observations from the CaHK filter of the MegaPrime/MegaCam on the CFHT, in combination with the broad-band optical and near infrared photometry of COSMOS. We surveyed 1.010 deg^2 of sky to $m_{\text{HK}} \sim 26$, approximately 5 orders of magnitude deeper than the *Pristine* survey (Starkenburg et al. 2017).

1,772 stars were retained from the initial *LAMPSS* catalogue of 62,652 sources after removing entries with undetermined u, g, r, i, z or m_{HK} and removing galaxies (with 70% completion and 30% contamination). Colour conditions for different $[\text{Fe}/\text{H}]$ values were found by creating metallicity-sensitive colour-colour diagrams using a range of data from POLLUX. From these conditions, 16 stars of $[\text{Fe}/\text{H}] \lesssim -3.0$ were identified.

One star, LAMPSS_1229 (see Figure 15), was found to have $[\text{Fe}/\text{H}] \sim -5.0$. LAMPSS_1229 falls in the ($g - i$) bin of G type stars and lies within the stellar halo at a distance from Earth of $78 \pm 9 \text{ kpc}$. These sources were confirmed as stars by manually checking *HST* imagery for each RA and Dec. A second G type star, LAMPSS_1586, was found to have a metallicity of $[\text{Fe}/\text{H}] \sim -3.0$. It was found to have a distance of $120 \pm 20 \text{ kpc}$, just within the stellar Halo. The lifetimes of LAMPSS_1229 and LAMPSS_1586, determined from their distances and apparent magnitude (Equation ??), is given by $8.29 \pm 1.43 \text{ Gyrs}$ and $10.86 \pm 2.87 \text{ Gyrs}$ respectively. This is surprising as LAMPSS_1586 has a longer lifetime than LAMPSS_1229, even though LAMPSS_1586 has a metallicity of -3.0 compared to -5.0. A lower metallicity star should have a greater lifetime if it was created in the early Universe. For LAMPSS_1229, we would expect a lifetime $> 11 \text{ Gyrs}$ (Starkenburg et al. 2018), however its approximated lifetime was far less than this. This is probably be-

cause LAMPSS_1229 is a sub-giant, so has a more negative apparent magnitude than calculated, therefore Equation ?? cannot be accurately used to determine its lifetime.

Several limitations affected the project. Firstly, when working out the magnitude cuts as shown in Figure 3, we found a value of $m_{\text{HK}} = 26$, however the actual drop-off magnitude was $m_{\text{HK}} = 25.3$. Secondly, when manually removing galaxies shown in §4.5, some galaxies would be behind the stars affecting their emission data, we therefore could not use this star. This reduces our completeness, as some stars could not be included in our sample. The conditions created to determine metallicities were created using a main sequence star model. This means that all results acquired are only valid for main sequence stars and further processes would need to be carried out to come up with estimates for non-main sequence stars. This is explained further in §8.

Additionally, the CaHK filter was not normalised (see Figure 2). However, the difference in area between the normalised and un-normalised was such that it only affected calculated magnitudes by a factor of a hundredth. If anything, this error would lead to conservative $[\text{Fe}/\text{H}]$ estimates. Therefore, due to time constraints, and the minimal effect on our EMP star sample, we chose not to correct this.

Overall, we present a sample of potentially EMP stars and one UMP star within the stellar halo obtained by analysing CaHK lines. We find a correlation between our results and the parallel study conducted by *WARP* (Jenkins et al. 2019). All metal-poor candidates identified require spectroscopic follow up, especially due to the uncertainties in the true metallicities of all K type *LAMPSS* stars discovered from extrapolation of metallicity conditions.

8 IMPROVEMENTS

In our methodology, we concentrated on Calcium II absorption lines, whereas other surveys such as Starkenburg et al. (2018) used Na I (Sodium), Mg I (Magnesium), Si I (Silicon), Ca I (Calcium), Fe I (Iron) and Ti II (singly ionised Titanium). Using more element absorption lines means we could be more confident in our metallicity data, as we would expect the abundance of any metals to increase the metallicity. Therefore in a metal-poor star, all these elements should be of little abundance rather than just one. Equally knowing the carbon abundance in a star would help avoid situations such as the one described in §2.2.

Furthermore, spectroscopic data would allow the lithium abundance of proposed metal-poor stars to be determined, a particularly useful piece of information because stars with a metallicity $[\text{Fe}/\text{H}] < -3$ will contain an amount of lithium below the ‘Spite Plateau’, a baseline of constant lithium abundance of ≈ 2.26 (Fu et al. 2015) which features in less evolved, higher metallicity stars ($[\text{Fe}/\text{H}] \leq 3$).

In addition, we assumed that all stars observed were in their main sequence, however in reality some of these stars may be subgiants, but without knowing the radius of the stars, we cannot determine whether this is true. If the radius was known, instead of having to estimate it, we could plot a HR diagram and determine the stars stage in its lifetime. A star on main sequence at of 1.0 kpc of radius $1.0 R_{\odot}$ at Temperature of 5000 K, will therefore look like a subgiant

of radius $2.0 R_{\odot}$ at a distance of 2.0 kpc as their magnitudes for g , for example, will be the same. This will also change the metallicity of the star, as stars with masses between $0.8 M_{\odot}$ and $8 M_{\odot}$ (K and G type stars) have non-convective cores, therefore during their SubGiant Branch (SGB) the core has exhausted itself of hydrogen, and begins Hydrogen shell burning. The next step in this stars evolution will be the first dredge up, which will cause fusion products in the core to be brought to the surface, thus increasing the metallicity of the star. This is a problem as stars that have low metallicities (-5, -4 etc) will appear as higher metallicities (-2, -1 etc), and therefore will be ignored.

ACKNOWLEDGMENTS

The authors are thankful to CFHT for performing the observations, the COSMOS survey for resulting in such a rich photometric set of data and David Sobral for his considerable guidance throughout the project. This work is based in part on data from the POLLUX database (<http://pollux.graal.univ-montp2.fr>) operated at LUPM (Université Montpellier - CNRS, France with the support of the PNPS and INSU. We have benefited immensely from the public available programming language PYTHON, including NUMPY & SCIPY (Van Der Walt et al. 2011; Jones et al. 2001), MATPLOTLIB (Hunter 2007), ASTROPY (Astropy Collaboration et al. 2013) and the TOPCAT analysis program (Taylor 2013). This research has also made use of the VizieR catalogue access tool, CDS, Strasbourg, France. We are also grateful for all of Lancaster University's on-campus caffeine dispensaries.

REFERENCES

- Arnould M., Goriely S., Takahashi K., 2007, *Physics Reports*, 450
 Astropy Collaboration et al., 2013, *A&A*, 558, A33
 Battaglia G., et al., 2005, *MNRAS*, 364, 433
 Becerra F., Greif T. H., Springel V., Hernquist L. E., 2015, *MNRAS*, 446, 2380
 Beers T. C., Christlieb N., 2005, *ARA&A*, 43, 531
 Bromm V., Coppi P. S., Larson R. B., 1999, *ApJ*, 527, L5
 Bromm V., Coppi P. S., Larson R. B., 2002, *The Astrophysical Journal*, 564, 23
 Caffau E., et al., 2011, *Nature*, 477, 67
 Capak P., et al., 2007, *ApJS*, 172, 99
 Carrera R., Gallart C., Pancino E., Zinn R., 2007, *AJ*, 134, 1298
 Chiti A., Frebel A., 2019, arXiv e-prints,
 Forbes D. A., et al., 2018, arXiv e-prints, pp 4–6
 Fu X., Bressan A., Molaro P., Marigo P., 2015, *MNRAS*, 452, 3256
 Griffen B. F., Dooley G. A., Ji A. P., O'Shea B. W., Gómez F. A., Frebel A., 2018, *MNRAS*, 474, 443
 Hansen T. T., et al., 2018, *ApJ*, 858, 92
 Hartwig T., Bromm V., Klessen R. S., Glover S. C. O., 2015, *MNRAS*, 447, 3892
 Hartwig T., Bromm V., Loeb A., 2018, *MNRAS*, 479, 2202
 Hubble E., 1929, *Proceedings of the National Academy of Science*, 15, 168
 Hunter J. D., 2007, *Computing In Science & Engineering*, 9, 90
 Ishiyama T., Sudo K., Yokoi S., Hasegawa K., Tominaga N., Susa H., 2016, *ApJ*, 826, 9
 Jenkins A., Wragg F., Butterworth J., Edwards J., O'Neill C., Gough J., Sobral D., 2019, *NLUAstro*, 1, 21

- Jones E., Oliphant T., Peterson P., et al., 2001, SciPy: Open source scientific tools for Python, <http://www.scipy.org/>
 Keller S. C., et al., 2014, *Nature*, 506, 463
 Koh D., Wise J. H., 2018, *MNRAS*, 474, 3817
 Laughlin G., Bodenheimer P., Adams F. C., 1997, *ApJ*, 482, 420
 Lemaître G., 1927, *Annales de la Société Scientifique de Bruxelles*, 47, 49
 M. Magg Klessen R., Glover S., H. L., 2019,
 Macaulay E., et al., 2018, arXiv e-prints,
 Magg M., Hartwig T., Agarwal B., Frebel A., Glover S. C. O., Griffen B. F., Klessen R. S., 2018, *MNRAS*, 473, 5308
 Nordlander T., Amarsi A. M., Lind K., Asplund M., Barklem P. S., Casey A. R., Collet R., Leenaarts J., 2017, *A&A*, 597, A6
 Oke J. B., 1974, *ApJS*, 27, 21
 Oke J. B., Gunn J. E., 1983, *ApJ*, 266, 713
 Placco V. M., Beers T. C., Reggiani H., Meléndez J., 2016a, *ApJ*, 829, L24
 Placco V. M., et al., 2016b, *ApJ*, 833, 21
 Ryan S., Norton A., 2010, *Stellar Evolution and Nucleosynthesis*. Cambridge University Press, <https://books.google.co.uk/books?id=PE4yGiU-JyEC>
 Sakari C. M., et al., 2018, *ApJ*, 868, 110
 Sarmento R., Scannapieco E., Cohen S., 2018, *ApJ*, 854, 75
 Schaefer D., 2002, *A&A*, 382, 28
 Scharping N., 2017, D-brief
 Scoville N., et al., 2007, *ApJS*, 172, 1
 Sestito F., et al., 2019, *MNRAS*, 484, 2166
 Stacy A., Bromm V., Lee A. T., 2016, *MNRAS*, 462, 1307
 Starkenburg E., et al., 2017, *MNRAS*, 471, 2587
 Starkenburg E., et al., 2018, *MNRAS*, 481, 3838
 Taylor M., 2013, *Starlink User Note*, 253
 Trenti M., Padoan P., Jimenez R., 2015, arXiv e-prints, pp 1–5
 Van Der Walt S., Colbert S. C., Varoquaux G., 2011, *Computing in Science & Engineering*, 13, 22
 Vásquez S., Zoccali M., Hill V., Gonzalez O. A., Saviane I., Rejkuba M., Battaglia G., 2015, *A&A*, 580, A121
 Weidner C., Vink J. S., 2010, *A&A*, 524, A98

This paper has been typeset from a $\text{\TeX}/\text{\LaTeX}$ file prepared by the author.